On Mapping Local Foam Mobility in Porous Media from Computer Tomography Data

Chapiro, G.; Quinelato, T. O.; Pereira, W.; dos Santos, R. W.; Zitha, P. L.J.

DOI
10.2118/223115-PA

Publication date
2024

Document Version
Final published version

Published in
SPE Journal

On Mapping Local Foam Mobility in Porous Media from Computer Tomography Data

G. Chapiro[1]*, T. O. Quinelato[2], W. Pereira[3], R. W. dos Santos[1], and P. L. J. Zitha[4†]

[1]Federal University of Juiz de Fora
[2]Federal University of Paraná
[3]National Renewable Energy Laboratory
[4]Delft University of Technology

Summary

Recovering apparent viscosity and foam texture fields from coreflooding experiments is challenging, even with modern computer tomography (CT) scan equipment. In this work, we present an explicit expression for efficiently calculating effective foam viscosity and propose an improved procedure for processing CT scan images to obtain accurate water saturation profiles. Using these techniques, we processed data from a CT scan of a coreflooding experiment, showing that the increase in effective foam viscosity due to foam generation occurs early during injection and before breakthrough. The fast increment in apparent viscosity is due to foam generation before breakthrough. After breakthrough, foam texture reaches its maximum, and effective foam viscosity grows logarithmically over time as the foamed gas sweeps out the water phase. The pressure drop obtained by using the effective foam viscosity showed good agreement with the experimentally obtained values before breakthrough. The workflow proposed here could be readily adapted to other foam models, provided reasonable estimates for these new quantities can be determined from experiments.

Introduction

The significance of foam as a method for controlling gas mobility and thus improving its sweep efficiency has been highlighted by many past studies concerning enhanced oil recovery (Casteel and Djabbarah 1988; Aarra et al. 2002), acid diversion during matrix stimulation (Behenna 1995), contaminated aquifer remediation (Burman and Hall 1986), and CO_2 storage into aquifers and depleted gas or oil fields (Eide et al. 2020; Sæle et al. 2022). The ability of foam to improve the sweep efficiency depends on its strength and stability. This results from a balance of foam generation and destruction mechanisms, which are controlled by several factors, such as the nature of the gas and the surfactant, rock matrix properties, and fluid-fluid and solid-fluid interactions (Casteel and Djabbarah 1988; Vikingstad et al. 2006; Almajid and Kovscek 2016).

In addition to pressure and flow measurements, in recent years, CT scan images have been used to obtain information on foam flow in coreflooding experiments, such as gas front position. In recent years, the design and execution of experiments involving CT imaging have evolved from a very challenging mode to a more established process building on previous findings and sufficient existing insights (Chen et al. 2010; Almajid et al. 2019). Recent works reporting CT scan imaging of foam flow in porous media show good agreement with pressure measurements (Du et al. 2008; Simjoo and Zitha 2015) and mathematical modeling (Zavala et al. 2022). This work proposes a workflow to use CT scan images to deduce foam flow properties, such as effective foam viscosity distribution and pressure profiles along the core.

Surfactant-stabilized foam has often been reported to flow through porous media like a shear-thinning fluid (Marsden and Khan 1966; Hirasaki and Lawson 1985; Heller and Kuntamukkula 1987; Khatib et al. 1988; Falls et al. 1989; Singh et al. 1997; Zitha and Du 2010; Fernø et al. 2016), meaning that effective foam viscosity decreases as shear rate increases. A formula by Hirasaki and Lawson (1985) was validated against laboratory experiments and is currently the most used in population-based models (Thorat and Bruining 2016; Izadi and Kam 2019; Eide et al. 2020), for example, to relate foam velocity with its viscosity. It states (Eq. 1) that relative to the no-foam viscosity, the increment of foam effective (and, consequently, apparent) viscosity in capillary tubes is proportional to the $-1/3$ power of foamed gas velocity when the film thickness is either negligible or very large, which describes foam as a shear-thinning material. The coefficient $c = 1/3$ is consistent with the classical result of Bretherton (1961). The formula and experiments in Hirasaki and Lawson (1985) verify that the proportionality relation holds at low injection rates and that, for higher rates, the exponent changes to $c = 2/3$. In this work, we write Hirasaki and Lawson's expression for the effective foam viscosity μ_f as

$$\mu_f = \mu_g^0 + \frac{\alpha n_f}{v_g^c}, \qquad c \in \{1/3, 2/3\}, \tag{1}$$

where μ_g^0 is the gas viscosity in the absence of foam, n_f is the foam texture (usually defined as the number of bubbles per unit volume), v_g is the interstitial velocity of the flowing gas phase, and α is a proportionality constant.

Effective foam viscosity is directly connected to the mobility reduction factor, which describes how the presence of foam impacts the gas phase mobility. Both quantities are essential to describing foam flow in porous media and are reported in numerical simulations (Farajzadeh et al. 2016; Ding et al. 2020). Since foamed gas velocity depends on the effective foam viscosity, Eq. 1 is an implicit equation in μ_f; furthermore, calculating these variables is quite challenging (Kam et al. 2007). Similar difficulties appear if one seeks to obtain

*Corresponding author; email: grigorichapiro@gmail.com

†Deceased

Original SPE manuscript received for review 30 March 2024. Revised manuscript received for review 02 August 2024. Paper (SPE 223115) peer approved 19 August 2024.

apparent foam viscosity (i.e., the observed viscosity of the fluid mixture) from experimental data. In the first part of this work, we follow the papers (da Silva Pereira and Chapiro 2023; Cedro and Chapiro 2024) and solve Eq. 1 for a two-phase flow model of foam in porous media, and the main remaining unknowns are gas saturation (S_g), foam texture (n_f), gradient of capillary pressure (∇P_c), and total superficial velocity (u). The result is an explicit expression for μ_f that, while equivalent to Eq. 1, does not require iterative implementations. A direct implementation could reduce computational time and numerical errors. We also show the applicability of the explicit expression for μ_f presenting the post-processing of CT scan data to obtain an estimate for the spatial distribution of foam apparent viscosity.

Foam has a remarkable ability to increase the trapped gas saturation in a porous medium, as first noted by Fried (1961). Several studies (Falls et al. 1989; Kovscek et al. 1994; Kovscek and Bertin 2003; Jones et al. 2018) later identified the effect of gas trapping by foam as the primary mechanism responsible for the increased apparent viscosity of foam. In fact, gas trapping contributes to the diversion of fluid to less permeable regions of heterogeneous reservoirs, increasing sweep efficiency. Matrix acidization can also benefit from gas trapping, as noted by Kovscek and Bertin (2003) and Nguyen et al. (2009b). The measurement of the quantity of gas trapped by foam is usually done with tracers, either by quantifying the amount of tracer in the effluent (Radke and Gillis 1990; Friedmann et al. 1991; Tang and Kovscek 2006) or by imaging (Tang and Kovscek 2006; Nguyen et al. 2009a; Kil et al. 2011; Jones et al. 2018). In this work, we use an explicit expression to investigate the increment of effective foam viscosity and its relation to foam generation during coreflooding experiments.

Mathematical Model for Foam Dynamics

Major mechanistic models describing foam flow in the porous medium are based on the same principle of how the foam texture affects fluid mobilities. This paper focuses on the effective foam viscosity, which is a common property to the existing models reported in the literature (Kovscek et al. 1994; Zitha 2006; Kam et al. 2007; Rossen 2013).

The main governing equations for modeling the flow of two immiscible phases of foam flow in a porous medium are the mass conservation and the generalized Darcy's laws of each phase. Following Chen and Ewing (1997), they are written as

$$u_w = \frac{\lambda_w}{\lambda_w + \lambda_g}(u + \lambda_g K(\nabla P_c - (\rho_g - \rho_w)\boldsymbol{g})), \tag{2}$$

$$u_g = \frac{\lambda_g}{\lambda_w + \lambda_g}(u - \lambda_w K(\nabla P_c - (\rho_g - \rho_w)\boldsymbol{g})), \tag{3}$$

where K is the permeability, $u = u_w + u_g$ is the total superficial velocity, $P_c = P_c(S_w)$ is the capillary pressure, $\boldsymbol{g}$ is the gravity vector field, and ρ_i, u_i, λ_i, and S_i are the mass density, superficial velocity, relative mobility, and saturation of phase $i \in \{w, g\}$. We use the subscript "w" for the wetting (aqueous) phase and "g" for the gas phase. Moreover, it is usual to define the relative phase mobilities as

$$\lambda_w = \frac{k_{rw}}{\mu_w}, \qquad \lambda_g = \frac{k_{rg}}{\mu_f}, \tag{4}$$

where k_{rw} is the water relative permeability, k_{rg} is the gas relative permeability, μ_w is the water viscosity, and μ_f is the effective foam viscosity.

Foam strength is a key property to understanding foam's influence on gas mobility, which is usually associated with how foam presence reduces gas mobility. Some models, known as implicit texture models, associate this property directly with other quantities, such as phase saturation, the concentration of the foaming agent, and phase velocities (Rossen 2013). On the other hand, the explicit texture models associate foam strength with the foam texture in the gas phase, denoted by n_f, either using balance equations for foam texture or considering local equilibrium expressions for this quantity. In any of these cases, it is useful to define the dimensionless foam texture, n_D, as

$$n_D = n_f / n_{\max}, \tag{5}$$

where $n_{\max}$ is the reference foam texture.

Some auxiliary physical quantities are equally important in this work. We define a normalized water saturation, S_{we}, as

$$S_{we} = \frac{S_w - S_{wc}}{1 - S_{wc} - S_{gr}}, \tag{6}$$

where S_{wc} is the connate water saturation, and S_{gr} is the residual gas saturation. The velocity of the fluid mixture is written as

$$u = -K(\lambda_w + \lambda_g)\left(\nabla P - \frac{\lambda_g \rho_g + \lambda_w \rho_w}{\lambda_w + \lambda_g}\boldsymbol{g}\right), \tag{7}$$

where P is the global pressure defined as (Chavent and Jaffr 1986; Chen and Ewing 1997)

$$P = P_g - \int_{1-S_{gr}}^{S_w} \frac{\lambda_w}{\lambda_w + \lambda_g}\frac{\mathrm{d}P_c}{\mathrm{d}\xi}\,\mathrm{d}\xi, \tag{8}$$

with P_g denoting the gas pressure. The global pressure can be interpreted as the pressure of the mixture, in this case, water and gas. Finally, the interstitial velocity of phase i is

$$v_i = \frac{|u_i|}{\phi S_i}, \qquad i \in \{w, g\}. \tag{9}$$

An Explicit Expression for Foam Viscosity

Hirasaki and Lawson (1985) proposed the formula in Eq. 1 for the shear-thinning effective foam viscosity. The proportionality constant α depends on many factors, including pore structure, liquid viscosity, and gas-liquid surface tension (Hirasaki and Lawson 1985). Due to the inherent difficulty of obtaining α, many authors use it as a fitting parameter, for example, Kovscek et al. (1995), Kam (2008), Thorat and Bruining (2016), Eide et al. (2020), and Simjoo and Zitha (2020). Since v_g itself depends on μ_f (see Eqs. 3, 4, and 9), Eq. 1 defines μ_f implicitly as

$$\mu_f = \mu_g^0 + \alpha n_f \left(\frac{\phi S_g}{k_{rg} \mid u - \lambda_w K(\nabla P_c - (\rho_g - \rho_w)\mathbf{g}) \mid} \right)^c (k_{rg} + \lambda_w \mu_f)^c, \tag{10}$$

where $c \in \{1/3, 2/3\}$. In fact, one may use the variable $X = (k_{rg} + \lambda_w \mu_f)^{1/3}$ to rewrite Eq. 10 as the cubic polynomial in X:

$$Q(X) = X^3 - \alpha n_f \lambda_w \left(\frac{\phi S_g}{k_{rg} \lvert u - \lambda_w K(\nabla P_c - (\rho_g - \rho_w)\mathbf{g}) \rvert} \right)^c X^{3c} - \left(k_{rg} + \lambda_w \mu_g^0 \right). \tag{11}$$

The procedure for solving cubic equations dates from the 16th century and is known as Cardano's formula (see Appendix A). Here, we follow da Silva Pereira and Chapiro (2023) and restrict ourselves to physically admissible solutions X to Eq. 11, which, in this case, means that $\mu_f = (X^3 - k_{rg})/\lambda_w \geq \mu_g^0 > 0$. Before obtaining the solutions for Eq. 11, we should discuss the types of solutions this equation has. We use the inflection points of Q and the signs of $Q(X)$ to this end. First, observe that $Q'(X) = 0$ if, and only if,

$$X^{3(1-c)} = c\alpha n_f \lambda_w \left(\frac{\phi S_g}{k_{rg} \lvert u - \lambda_w K(\nabla P_c - (\rho_g - \rho_w)\mathbf{g}) \rvert} \right)^c. \tag{12}$$

Since the right side of the last expression is non-negative and $3(1-c) \in \{1, 2\}$, Q has at most one positive inflection point. Moreover, one can easily verify that $Q(0) < 0$ and $\lim_{X \to +\infty} Q(X) = +\infty$, from which we conclude $Q(X)$ has a unique positive root.

Now, we use the formulas from Zwillinger (2002, §2.3.2) to characterize the single positive root of Eq. 11. For that, we define

$$a_c = \frac{\alpha n_f \lambda_w}{3} \left(\frac{\phi S_g}{k_{rg} \mid u - \lambda_w K(\nabla P_c - (\rho_g - \rho_w)\mathbf{g}) \mid} \right)^c, \qquad b = \frac{k_{rg} + \lambda_w \lambda_g^0}{2}, \tag{13}$$

where c is either 1/3 or 2/3. Using these formulas, we can rewrite Eq. 10 as

$$\mu_f = \begin{cases} \mu_g^0 + \dfrac{3a_c}{\lambda_w} \left(\sqrt[3]{b + \sqrt{b^2 - a_c^3}} + \sqrt[3]{b - \sqrt{b^2 - a_c^3}} \right) & \text{if } c = 1/3, \\ \mu_g^0 + \dfrac{3a_c}{\lambda_w} \left(\sqrt[3]{(a_c^3 + b) + \sqrt{2a_c^3 b + b^2}} + \sqrt[3]{(a_c^3 + b) - \sqrt{2a_c^3 b + b^2}} \right) & \text{if } c = 2/3. \end{cases} \tag{14}$$

Here, $\sqrt[3]{y}$ denotes either the real cube root, when $y \in \mathbb{R}$, or the principal cube root, when $y \in \mathbb{C}$. Therefore, the terms inside the parentheses are the unique positive roots of $Q(X)$. Moreover, Eq. 14 always delivers a positive expression for μ_f that satisfies $\mu_f \geq \mu_g^0$. The right side of Eq. 14 is an explicit function of u, n_f, S_w, and ∇S_w since λ_w, k_{rg}, and P_c depend on S_w.

Notice that, when $u_g = 0$ (see Eq. 3), a_c is undefined. In this case, both Eqs. 1 and 14 are invalid. Nonetheless, it is usual to assume that $\mu_f = \mu_g^0$ when only the aqueous phase is flowing.

Experiments

As already mentioned, one of the goals of this work is to illustrate the application of the explicit effective viscosity formula by analyzing the coreflooding experiments reported by Simjoo and Zitha (2015). A brief overview of the experiments follows. We confine the discussion to the essential aspects needed to render this work self-contained and refer the reader to Simjoo and Zitha (2015) for details.

The experiments consist of the coinjection of the alpha olefin sulfonate surfactant dissolved in brine and nitrogen into cylindrical Bentheimer sandstone cores having 3.8 cm diameter and 38.4 cm length. The properties of fluids and porous media used in the experiments are given in **Table 1**. The cores were previously saturated with the same surfactant solutions using the procedure described in Simjoo and Zitha (2015). Then, the surfactant solution and the nitrogen gas were coinjected.

Parameter	Symbol	Value
Foam exponent	c	1/3 (-)
Magnitude of gravity acceleration	g	9.8 (m/s^2)
Gas endpoint permeability	k_{rg}^0	1 (-)
Water endpoint permeability	k_{rw}^0	0.75 (-)
Maximum foam texture	$n_{\max}$	5.0×10^{11} (1/m^3)

Table 1—Parameters in the foam model.

Parameter	Symbol	Value
Entry capillary pressure	P_c^0	1.2×10^4 (Pa)
Residual gas saturation	S_{gr}	0.0 (-)
Connate water saturation	S_{wc}	0.1 (-)
Injection superficial velocity	U_{inj}	1.617×10^{-5} (m/s)
Proportionality constant	α	7×10^{-16} (Pa·s$^{2/3}$m$^{10/3}$)
Water viscosity	μ_w	10^{-3} (Pa·s)
Gas viscosity in the absence of foam	μ_g^0	1.8×10^{-5} (Pa·s)
Corey model exponent	λ	5 (-)
Water mass density	ρ_w	10^3 (kg/m^3)
Gas mass density	ρ_g	1.165 (kg/m^3)
Cap. pressure coefficient	γ	0.5 (-)

Table 1 (continued)—Parameters in the foam model.

During foam development, pressure drops were measured over a certain number of core sections along the length of the core, and the core was CT scanned to visualize and quantify the local fluid saturations over time. The CT scan images were obtained using a third-generation medical scanner, providing a minimum voxel size of 0.3×0.3×1.0 mm^3 and a minimum slice scan time smaller than 5 seconds. The core sample was cast within a self-hardening resin (Araldite) layer and machined to fit precisely in a core holder made of polyetheretherketone, or PEEK, a synthetic material known for its superior mechanical properties. The resin and the core holder were chosen for their low X-ray attenuation.

CT scan settings were selected to minimize noise and inevitable artifacts, such as beam hardening and cross artifacts, with satisfactory results. Each CT scan image shows the local attenuation of the subject examined in Hounsfield units (H). A Hounsfield unit represents a 0.1% change in density with respect to a calibration density scale (Akin and Kovscek 2003). The CT scan images were processed and converted into porosity and aqueous phase saturation during foam flow using Avizo™ visualization and analysis software (Simjoo et al. 2013). The porosity is given by Vinegar and Wellington (1987)

$$\phi = \frac{H_{\text{dry}} - H_{\text{wet}}}{H_w}, \tag{15}$$

where H_{dry} and H_{wet} are the attenuations measured, respectively, for the dry core and for the core fully saturated with brine, and H_w is the brine attenuation.

Following Akin and Kovscek (2003), the porosity field can be estimated by

$$\phi = \frac{H_b - H_a}{H_w}, \tag{16}$$

where H_b and H_a denote, respectively, the CT numbers (normalized attenuation coefficients) corresponding to brine- and air-saturated core, and H_w = 1,000 H is the CT number of water. These quantities are given in Hounsfield units. During the foam coreflooding experiment, one can use

$$S_w = \frac{H_f - H_a}{H_s - H_a}, \tag{17}$$

to estimate the water saturation in each voxel (Simjoo et al. 2013), with H_f and H_s denoting the CT numbers measured in a core saturated with foam and with the surfactant solution, respectively.

New Procedure for Processing the CT Scan Data

The acquisition and preprocessing of raw X-ray attenuation data used in this article are described by Zitha et al. (2006). The images obtained from CT scan experiments were saved in the DICOM format (Eichelberg et al. 2004). In this paper, the CT scans were reprocessed using a slightly different method than the one used in Simjoo and Zitha (2015), enabling the absolute permeability field to be obtained directly from CT scan images, in addition to the porosity and saturations. The DICOM ToolKit library, V 3.6.5 (Eichelberg et al. 2004), and the OpenCV library, V 4.5.0 (Bradski 2000), were used to extract the relevant data from the DICOM files.

Each CT scan image represents a cross section of the core perpendicular to the scanning direction. They are stored in the DICOM file as a 512×512 matrix whose entries are the measured attenuation coefficients of the core and its surroundings. The following image segmentation procedure is used to isolate the voxels corresponding to the core from the ones corresponding to its surroundings: First, a volume of interest window of width 1 voxel and center at 1,040 is used to binarize the CT image; the binary voxel data are then scaled to a gray-scale color space stored in 8 bits; next, a Gaussian filter with 7×7 support and standard deviation of 1.5 in each direction is used to blur the binary image; the 21HT circle detection algorithm (Yuen et al. 1990), based on the Hough transform and implemented in the OpenCV library, is used with parameters 200 and 100 to detect in each slice a circle with a radius allowed to range from 95 to 110 pixels; the line segment that best approximates the centers of the detected circles (in the sense of least squares) is selected as the core axis, around which we collect a cylindrical region of 193 voxels diameter from the original images.

In this paper, we work with the 2D interpretation of the experimental data. In this case, the original voxel data inside the cylindrical region are extracted and grouped to reconstruct a longitudinal radial cut of the core. First, we compute the 2D porosity field using the

procedure described above (see Eq. 15); the permeability field is then computed using the Kozeny-Carman relationship (Dullien 2012; Urumović 2016)

$$K = \frac{\phi^3 D_m^2}{180(1-\phi)^2}, \tag{18}$$

where D_m is the mean grain diameter, considered constant for simplicity and estimated to be 1.45×10^{-4} m to fit the overall permeability (2.5 ± 0.1 darcy) reported by Simjoo and Zitha (2015). **Figs. 1 through 3** exhibit the porosity field, histogram of the porosity field, and the corresponding permeability field computed from CT scan images. **Fig. 4** presents the water saturation profiles at different times.

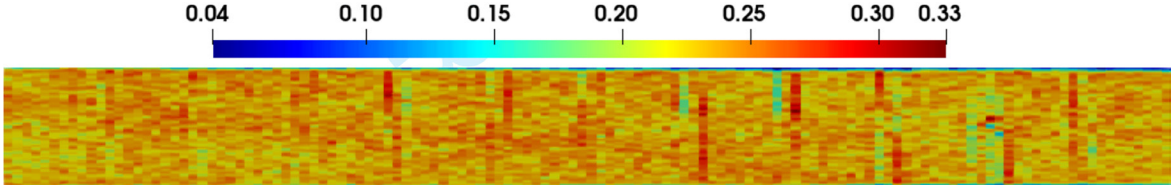

Fig. 1—Porosity field computed from CT images; the bottom of the core is on the left.

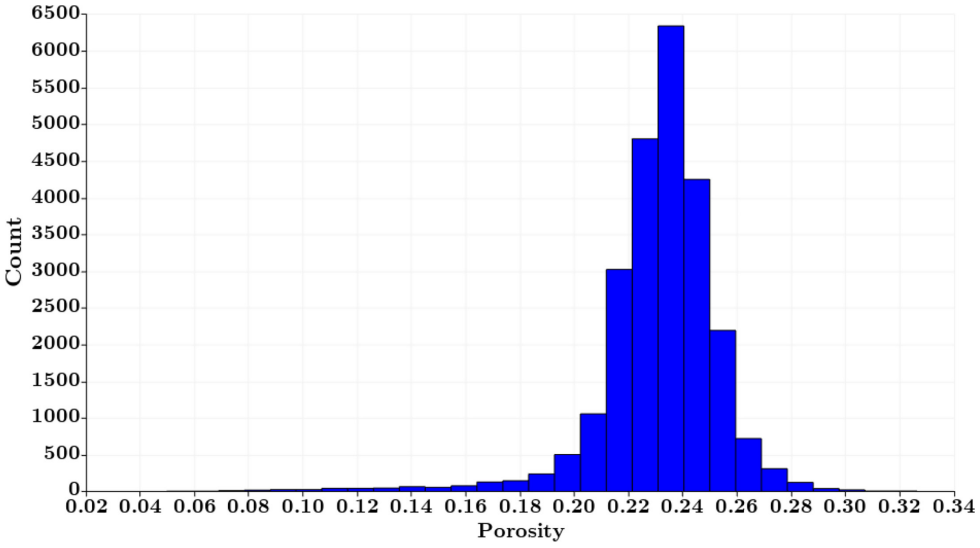

Fig. 2—Histogram of porosity field computed from CT images.

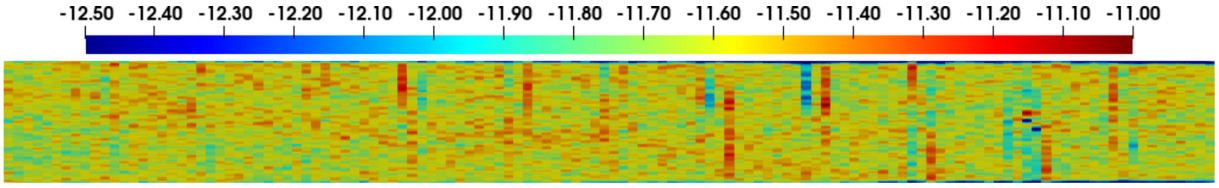

Fig. 3—Log_{10} of the permeability field obtained from the porosity field via a Kozeny-Carman relationship; the bottom of the core is on the left.

Notice that the presented methodology results in a precise and clear view of water saturation over time; see **Fig. 4**. The propagation of the gas front during the drainage process [0.03–0.67 pore volumes (PV)], the breakthrough (0.67 PV), and the slow counterflow water saturation wave (1.48–49.09 PV) is clearly visible and agrees with Simjoo and Zitha (2015).

Algorithm Summary and Practical Considerations. Let us summarize the proposed methodology for the computation of effective foam viscosity from CT scan images. The first step is to compute porosity and water saturation using Eqs. 16 and 17. Next, the permeability field is computed using porosity in Eq. 18. Finally, the effective foam viscosity μ_f is obtained from Eq. 14.

We assumed that foam was in local equilibrium during the experiment. Using the model by Simjoo and Zitha (2015), this means that $n_f = n_{\max}$ if $S_w < 1$, and, by convention, $n_f = 0$ if $S_w = 1$.

An approximation for the superficial velocity u is computed by using Eq. 7 and the mass balance equation for the gas/water mixture (which is here assumed incompressible, for simplicity):

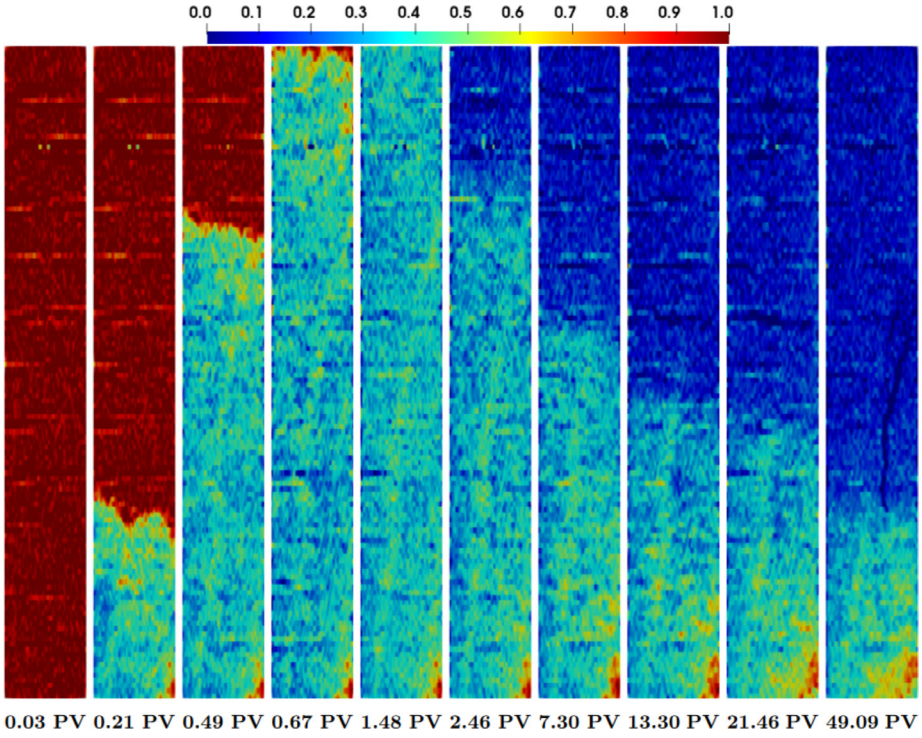

Fig. 4—Water saturation profile along the central vertical cross section (obtained from CT images). PV, pore volume.

$$\nabla \cdot u = 0. \tag{19}$$

The following iterative procedure was adopted:

1. Set $\mu_f = \mu_g^0$.
2. Compute u and P using Eqs. 7 and 19.
3. Update μ_f using Eq. 14.
4. If the computed quantities μ_f, u, and P converged, stop; otherwise, go to Step 2.

Results on Effective Gas Viscosity

We assume that ρ_w, ρ_g, μ_w, and μ_g^0 are known. **Table 1** lists all parameter values. The proportionality constant α was fitted to match the pressure profile reported by Simjoo and Zitha (2015). Moreover, k_{rw}, k_{rg}, and P_c are functions that depend solely on the effective water saturation S_{we} (Eq. 6):

$$\begin{aligned} k_{rw}(S_{we}) &= k_{rw}^0 S_{we}^{\lambda}, \\ k_{rg}(S_{we}) &= k_{rg}^0 (1 - S_{we})^{3+2\lambda}, \\ P_c(S_{we}) &= P_c^0 \gamma \left[\frac{0.5 - S_{wc}}{S_{we}(1 - S_{wc})} \right]^{1\lambda}. \end{aligned} \tag{20}$$

The gravity acts in the axial direction so that $\mathbf{g} = -g\mathbf{e}_x$, with $\mathbf{e}_x$ denoting a unit vector in the axial direction, from bottom to top. We use the chain rule to replace ∇P_c by $\frac{dP_c}{dS_w}\nabla S_w$ and a central difference scheme (except at boundary cells, where a forward—or backward—difference scheme is used) to compute an approximation for ∇S_w at each point.

Fig. 5 shows the effective gas viscosity during the injection process obtained using Eq. 14 at the same times as in **Fig. 4**. As the core starts with no gas, the initial effective gas viscosity is low and increases as the gas front advances. Effective gas viscosity increases rapidly during the injection with higher values in the water saturation front (around 10 cp or 10^{-2} Pa·s) and medium values (around 7.6 cp or 7.6 $\times 10^{-3}$ Pa·s) after it. After the breakthrough (0.67 PV), we observe that the counterflow water saturation front is connected to a significant increment in the effective foam viscosity and also the formation of a zone with high effective foam viscosity close to the injection end of the core.

Fig. 6 shows the foam viscosity histograms, that is, the relative frequencies of the value of foam viscosity in the flow domain. The overall histogram shows the full range of viscosity values, where a switch is observed from predominantly low (less than 1 mPa·s) to higher viscosity centered around 7.6 mPa·s before foam breakthrough and 8 mPa·s after breakthrough. The observed behavior supports the idea that the greatest increase in effective foam viscosity occurs during the initial propagation of the foam front through the core. The subsequent increase, associated with secondary core desaturation, is relatively small in comparison. Further scrutiny of the bubble distributions reveals several interesting features about the viscosity growth. From **Figs. 5 through 6**, we observe a rapid decay in the number of cells with low foam viscosity, with increasing average effective foam viscosity over time. This behavior is evident in the zoom of **Fig. 6**, where we plot part of the histogram. Up to 1.48 PV, the viscosity distribution function is bell-shaped, centered at approximately 7.6 mPa·s, as mentioned earlier. The following Gaussian function can describe the corresponding probability density function:

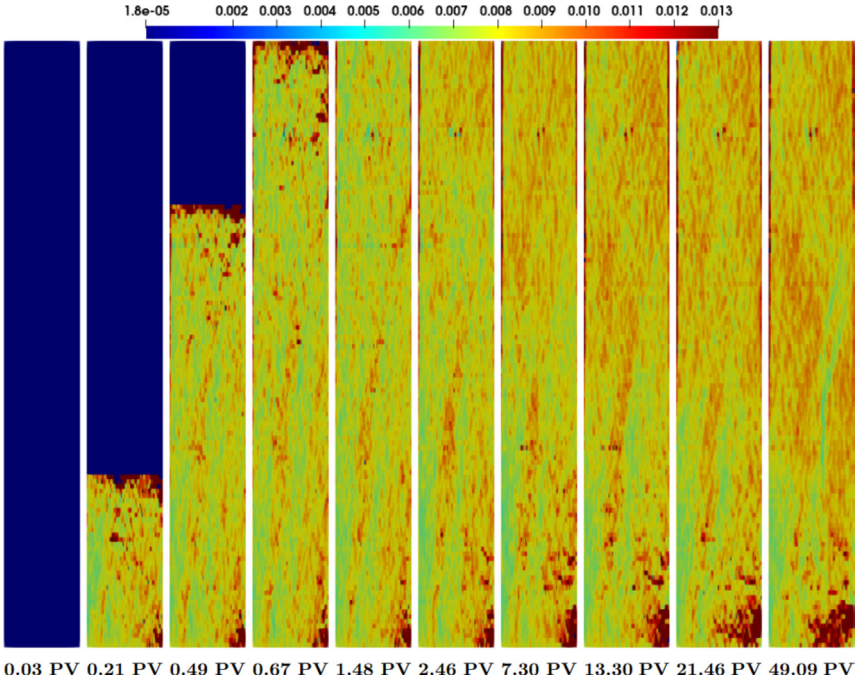

Fig. 5—Foam viscosity computed using Eq. 14.

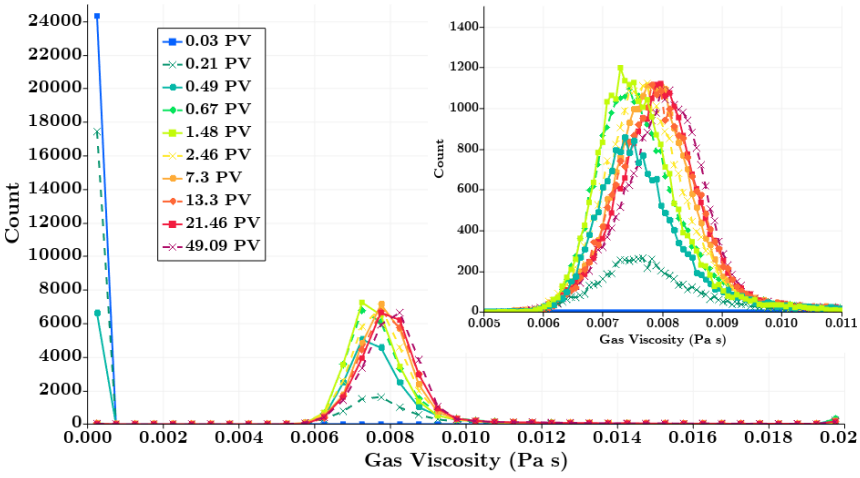

Fig. 6—Histogram showing the foam viscosity frequency in the core.

$$G(x) = \frac{1}{\sigma\sqrt{2\pi}} \exp\left[-\frac{(x-\mu)^2}{2\sigma^2}\right],$$

with computed means μ and variances σ shown in **Table 2**. However, the distribution is no longer symmetric for long dimensionless times (longer or equal to 7.3 PV in our case).

Several past works [e.g., Kovscek and Radke (1994)] report that the strong foam with high apparent viscosity is usually formed long after the breakthrough as we approach a steady-state foam. **Fig. 6** shows that the model predicts foam forming before the breakthrough.

Injected Volume (PV)	μ (Pa·s)	σ (mPa·s)
0.21	7.797×10^{-3}	9.140×10^{-4}
0.49	7.660×10^{-3}	7.729×10^{-4}
0.6	7.659×10^{-3}	7.816×10^{-4}
1.48	7.613×10^{-3}	7.251×10^{-4}

Table 2—Parameters of the Gaussian probability distribution functions that describe the effective foam viscosity.

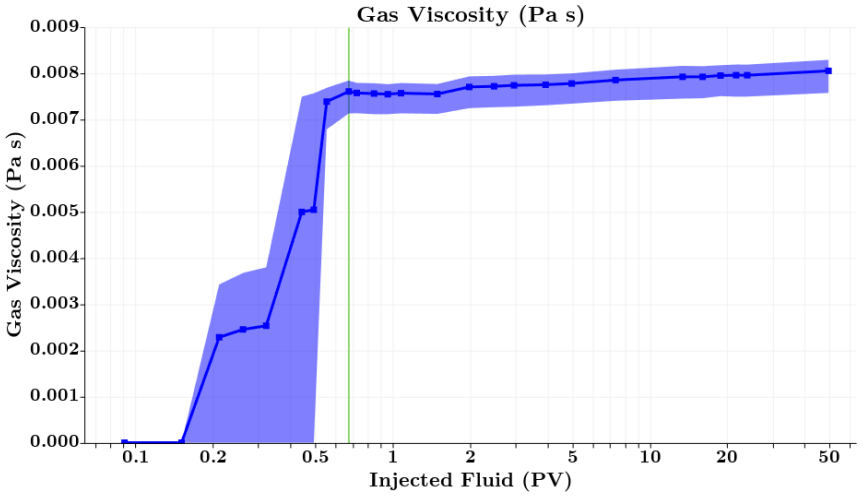

Fig. 7—The average gas viscosity (blue line) increases when the foam is created in the porous medium. The shaded region corresponds to the standard deviation, and the green line indicates gas breakthrough (approx. after the injection of 0.67 PV).

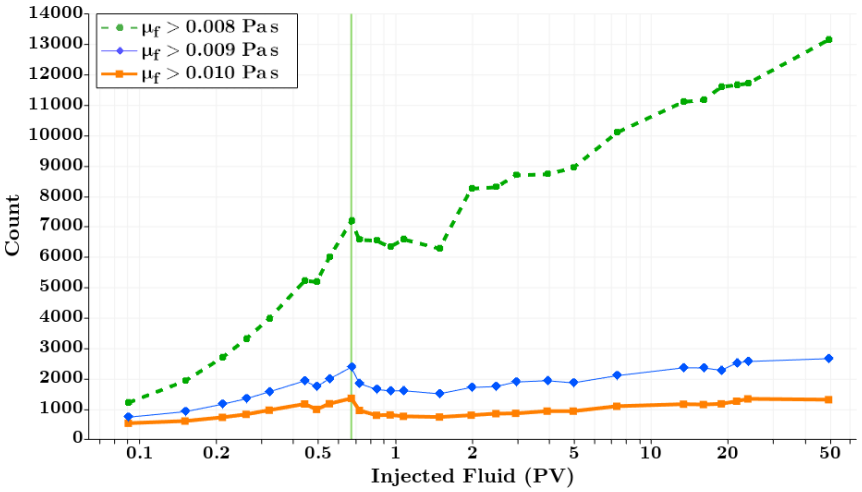

Fig. 8—Time evolution of the number of cells occupied by foam with viscosity greater than different thresholds. The vertical green line indicates gas breakthrough (approx. after the injection of 0.67 PV).

However, well aligned with previous works, we observe that the foam strength keeps increasing long after the breakthrough. We plot the average gas viscosity in **Fig. 7** to clarify these statements. In particular, this graph shows that gas viscosity increases much slower after breakthrough (notice we use log scale in the *x*-axis). Notice that the development of foam viscosity before breakthrough proceeds irregularly by jumps with transient plateaus. The authors attributed the stepwise increase of viscosity to intermittent foam generation and propagation. The exact mechanism of this behavior is not completely clear. However, the CT scan images (see **Fig. 7**) suggest that, before the breakthrough, foam is generated by bursts due to the heterogeneity of the cores. Similar behavior was observed in Lima et al. (2021) for microfluidic experiments for foam stabilized by sodium dodecyl sulfate.

To better understand the foam viscosity increment, we plot the number of cells evolution with effective viscosity over 8, 9, and 10 cp in **Fig. 8.** Notice that the corresponding frequency grows logarithmically (linearly in the semilogarithmic scale) after the breakthrough.

To better understand the observed physics, we plot the foam texture corresponding to the effective viscosity computed using Eq. 14, see **Fig. 9.** Notice that the foam texture reaches the maximum value before the breakthrough. Thus, the increment in effective viscosity observed in **Figs. 6 through 8** is due to the foamed gas filling the core and sweeping out of the water phase.

Finally, we integrate the effective foam viscosity, obtaining the total pressure drop along the core using Eq. 7. The results, plotted in **Fig. 10,** show good qualitative agreement between the pressure values estimated from CT scan images and the experimental values directly measured using piezometers (Simjoo 2012). The same procedure is used to obtain the pressure profiles after the breakthrough (see **Fig. 11**). We plot them here for completeness, as the corresponding experimentally obtained profiles were not reported in the literature. Thus, our approach is only validated before foam breakthrough.

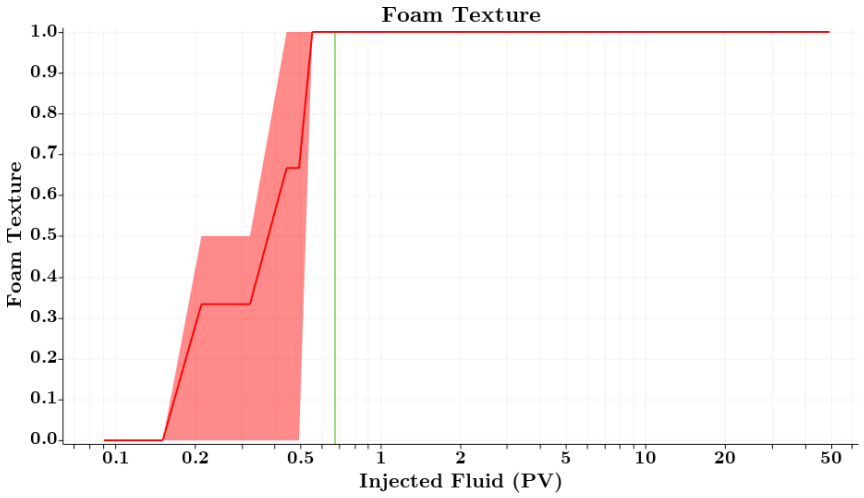

Fig. 9—The average foam texture (red line) increases when the foam is created in the porous medium. The shaded region corresponds to the standard deviation, and the green line indicates gas breakthrough (approx. after the injection of 0.67 PV).

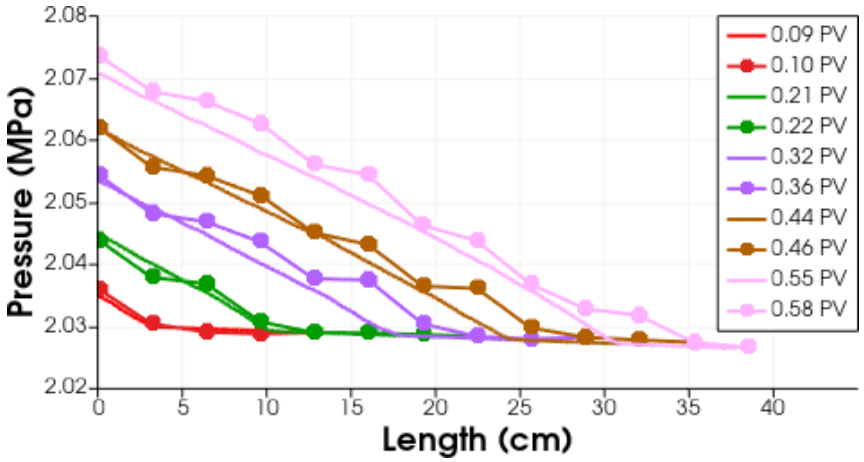

Fig. 10—Comparison between foam flooding pressure profiles obtained with CT scan images (solid lines) and experimental data from Simjoo and Zitha (2015) (circles).

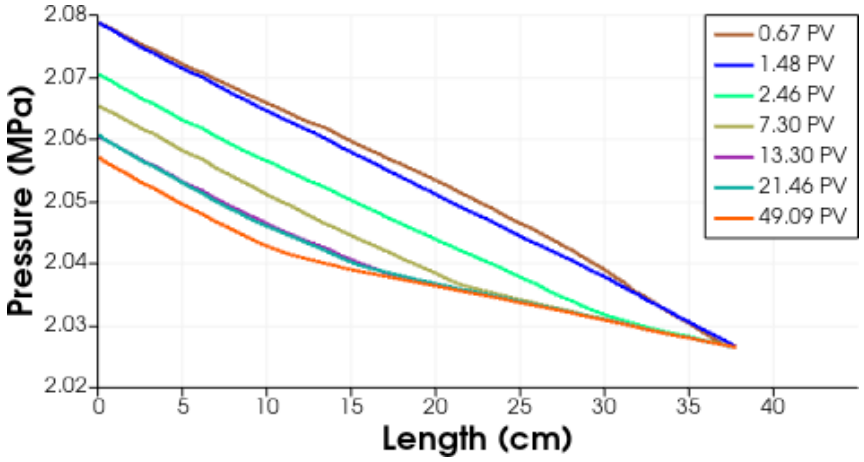

Fig. 11—Pressure profiles computed from CT scan images after breakthrough.

Discussions and Conclusions

- An explicit effective foam viscosity expression derived from the original Hirasaki-Lawson equation was successfully used to analyze the data reported in the literature. This expression depends on the total fluid velocity u, which is the volumetric flux of the fluid system

and can be estimated through initial and boundary measurements. Thus, the proposed effective viscosity equation is less sensitive to the dynamics than the original equation, which depends on the gas velocity varying from 0 to u.

- CT scan data were processed using a modified framework, allowing accurate water saturation profiles and porosity acquisition. We believe this procedure is especially interesting if applied to heterogeneous porous media and allows for the recovery of 3D velocity fields.
- We obtained histograms of the effective foam viscosity using the explicit effective viscosity equation and improved CT scan data processing. The histograms reveal that the greatest increase in viscosity occurs early during the injection (first 1.5 PV), beginning before the breakthrough (0.67 PV). After breakthrough, the viscosity distribution shifts from a Gaussian-like shape to a negatively skewed probability distribution (less symmetric). Moreover, the fast increment in the apparent viscosity is due to the foam generation, which happens before the breakthrough. After the breakthrough, the logarithmic increment in effective viscosity is due to the foamed gas sweeping out the water phase.
- The pressure drop calculated using the effective foam viscosity showed good agreement with the experimentally obtained values before the breakthrough. However, the approach presented in this paper is only validated before foam breakthrough. To our knowledge, there is still a need for a better understanding of the backward foam front propagation observed after the breakthrough. A successful approach to model this phenomenon requires adding a new quantity called the flowing foam fraction (Almajid et al. 2019). Nevertheless, the workflow proposed here could be readily adapted to other foam models, provided reasonable estimates for these new quantities can be determined from experiments.

Nomenclature

D_m = mean grain diameter [m]
g = gravity vector field [m/s^2]
H_{dry} = attenuation of the dry core [H]
H_{wet} = attenuation for the core saturated with brine [H]
H_w = brine attenuation [H]
K = permeability [m^2]
k_{rw} = water relative permeability [-]
k_{rg} = gas relative permeability [-]
n_D = dimensionless foam texture [-]
n_f = foam texture [1/m^3]
$n_{\max}$ = reference foam texture [1/m^3]
P = global pressure [Pa]
P_c = capillary pressure [Pa]
P_g = gas pressure [Pa]
u = total superficial velocity [m/s]
u_i = superficial velocity of phase $i \in$ {w,g} [m/s]
v_g = interstitial velocity of the flowing gas phase, [m/s]
S_g = gas saturation [-]
S_{gr} = residual gas saturation [-]
S_w = water saturation [-]
S_{wc} = connate water saturation [-]
S_{we} = normalized water saturation [-]
α = proportionality constant in foam viscosity [Pa·s$^{2/3}$m$^{10/3}$]
λ = Corey model exponent [-]
λ_i = relative mobility of phase i {w,g} [Pa^{-1}·s^{-1}]
μ_f = effective foam viscosity [Pa·s]
μ_g^0 = gas viscosity in the absence of foam, [Pa·s]
μ_w = water viscosity [Pa·s]
ϕ = porosity [-]
ρ_i = mass density of phase $i \in \{w,g\}$ [kg·m^{-3}]

Acknowledgments

The authors gratefully acknowledge support from Shell Brasil through the "Avançando na modelagem matemática e computacional para apoiar a implementação da tecnologia 'Foam-assisted WAG' em reservatórios do Pré-sal" ANP 23518-4 project at UFJF and the strategic importance of the support given by ANP through the R&D levy regulation. G.C. was supported in part by CNPq grants 306970/2022-8, 405366/2021-3, and FAPEMIG grant APQ-00405-21. This work was authored in part by the National Renewable Energy Laboratory, operated by Alliance for Sustainable Energy, LLC, for the U.S. Department of Energy (DOE) under Contract No. DE-AC36-08GO28308. The views expressed in the article do not necessarily represent the views of the DOE or the U.S. Government. The U.S. Government retains, and the publisher, by accepting the article for publication, acknowledges that the U.S. Government retains a nonexclusive, paid-up, irrevocable, worldwide license to publish or reproduce the published form of this work, or allow others to do so, for U.S. Government purposes.

References

Aarra, M. G., Skauge, A., and Martinsen, H. A. 2002. FAWAG: A Breakthrough for EOR in the North Sea. Paper presented at the SPE Annual Technical Conference and Exhibition, San Antonio, Texas, USA, 29 September−2 October. https://doi.org/10.2523/77695-MS.

Akin, S. and Kovscek, A. R. 2003. Computed Tomography in Petroleum Engineering Research. In *Applications of X-Ray Computed Tomography in the Geosciences*, eds. F. Mees, R. Swennen, and M. Van Geet, Vol. **215**, 23–38. London: Geological Society, London, Special Publications. https://doi.org/10.1144/GSL.SP.2003.215.01.03.

Almajid, M. M. and Kovscek, A. R. 2016. Pore-Level Mechanics of Foam Generation and Coalescence in the Presence of Oil. *Adv Colloid Interface Sci* **233**: 65–82. https://doi.org/10.1016/j.cis.2015.10.008.

Almajid, M. M., Nazari, N., and Kovscek, A. R. 2019. Modeling Steady-State Foam Flow: Hysteresis and Backward Front Movement. *Eng Fuels* **33** (11): 11353–11363. https://doi.org/10.1021/acs.energyfuels.9b01842.

Behenna, F. R. 1995. Acid Diversion from an Undamaged to a Damaged Core Using Multiple Foam Slugs. Paper presented at the SPE European Formation Damage Conference, The Hague, Netherlands, 15−16 May. https://doi.org/10.2523/30121-MS.

Bradski, G. 2000. The OpenCV Library. *Dr Dobbs J Softw Tools* **25** (11): 120–125.

Bretherton, F. P. 1961. The Motion of Long Bubbles in Tubes. *J Fluid Mech* **10** (2): 166. https://doi.org/10.1017/S0022112061000160.

Burman, J. W. and Hall, B. E. 1986. Foam as a Diverting Technique for Matrix Sandstone Stimulation. Paper presented at the SPE Annual Technical Conference and Exhibition, New Orleans, Louisiana, 5−8 October. https://doi.org/10.2118/15575-MS.

Casteel, J. F. and Djabbarah, N. F. 1988. Sweep Improvement in CO2 Flooding by Use of Foaming Agents. *SPE Res Eng* **3** (04): 1186–1192. https://doi.org/10.2118/14392-PA.

Cedro, J. B. and Chapiro, G. 2024. Traveling Wave Solutions for a Realistic Non-Newtonian Foam Flow Model. *Geoenergy Sci Eng* **232**: 212478. https://doi.org/10.1016/j.geoen.2023.212478.

Chavent, G. and Jaffr, J. 1986. *Mathematical Models and Finite Elements for Reservoir Simulation: Single Phase, Multiphase and Multicomponent Flows through Porous Media*, Vol. 17. North-Holland, Amsterdam: ASME.

Chen, Z. and Ewing, R. E. 1997. Fully Discrete Finite Element Analysis of Multiphase Flow in Groundwater Hydrology. *SIAM J Numer Anal* **34** (6): 2228–2253. https://doi.org/10.1137/S0036142995290063.

Chen, Q., Gerritsen, M. G. G., Kovscek, A. R. R. et al. 2010. Modeling Foam Displacement with the Local-Equilibrium Approximation: Theory and Experimental Verification. *SPE J.* **15** (1): 171–183. https://doi.org/10.2118/116735-PA.

da Silva Pereira, W. and Chapiro, G. 2023. Traveling Wave Solutions for Non-Newtonian Foam Flow in Porous Media. *Transp Porous Med* **148** (2): 247–265. https://doi.org/10.1007/s11242-023-01937-1.

Ding, L., Cui, L., Jouenne, S. et al. 2020. Estimation of Local Equilibrium Model Parameters for Simulation of the Laboratory Foam-Enhanced Oil Recovery Process Using a Commercial Reservoir Simulator. *ACS Omega* **5** (36): 23437–23449. https://doi.org/10.1021/acsomega.0c03401.

Du, D.-X., Beni, A. N., Farajzadeh, R. et al. 2008. Effect of Water Solubility on Carbon Dioxide Foam Flow in Porous Media: An X-Ray Computed Tomography Study. *Ind Eng Chem Res* **47** (16): 6298–6306. https://doi.org/10.1021/ie701688j.

Dullien, F. A. 2012. *Porous Media: Fluid Transport and Pore Structure*. San Diego, California: Academic Press.

Eichelberg, M., Riesmeier, J., Wilkens, T. et al. 2004. Ten Years of Medical Imaging Standardization and Prototypical Implementation: The DICOM Standard and the OFFIS DICOM Toolkit (DCMTK. In *Medical Imaging 2004: PACS and Imaging Informatics*, eds. O. M. Ratib and H. K. Huang, 57. Bellingham, Washington: SPIE. https://doi.org/10.1117/12.534853.

Eide, Ø., Fernø, M., Bryant, S. et al. 2020. Population-Balance Modeling of CO2 Foam for CCUS Using Nanoparticles. *J Nat Gas Sci Eng* **80**: 103378. https://doi.org/10.1016/j.jngse.2020.103378.

Falls, A. H., Musters, J. J., and Ratulowski, J. 1989. The Apparent Viscosity of Foams in Homogeneous Bead Packs. *SPE Res Eng* **4** (2): 155–164. https://doi.org/10.2118/16048-PA.

Farajzadeh, R., Eftekhari, A. A., Hajibeygi, H. et al. 2016. Simulation of Instabilities and Fingering in Surfactant Alternating Gas (SAG) Foam Enhanced Oil Recovery. *J Nat Gas Sci Eng* **34**: 1191–1204. https://doi.org/10.1016/j.jngse.2016.08.008.

Fernø, M. A., Gauteplass, J. ., Pancharoen, M. . et al. 2016. Experimental Study of Foam Generation, Sweep Efficiency, and Flow in a Fracture Network. *SPE J.* **21** (04): 1140–1150. https://doi.org/10.2118/170840-PA.

Fried, A. N. 1961. *The Foam-Drive Process for Increasing the Recovery of Oil*. Washington, D.C: U.S. Department of the Interior, Bureau of Mines.

Friedmann, F., Chen, W. H., and Gauglitz, P. A. 1991. Experimental and Simulation Study of High-Temperature Foam Displacement in Porous Media. *SPE Res Eng* **6** (01): 37–45. https://doi.org/10.2118/17357-PA.

Heller, J. P. and Kuntamukkula, M. S. 1987. Critical Review of the Foam Rheology Literature. *Ind Eng Chem Res* **26** (2): 318–325. https://doi.org/10.1021/ie00062a023.

Hirasaki, G. J. and Lawson, J. B. 1985. Mechanisms of Foam Flow in Porous Media: Apparent Viscosity in Smooth Capillaries. *Soc of Pet Eng J* **25** (02): 176–190. https://doi.org/10.2118/12129-PA.

Izadi, M. and Kam, S. I. 2019. Bubble-Population-Balance Modeling for Supercritical Carbon Dioxide Foam Enhanced-Oil-Recovery Processes: From Pore-Scale to Core-Scale and Field-Scale Events. *SPE Res Eval & Eng* **22** (04): 1467–1480. https://doi.org/10.2118/191202-PA.

Jones, S. A., Getrouw, N., and Vincent-Bonnieu, S. 2018. Foam Flow in a Model Porous Medium: II. The Effect of Trapped Gas. *Soft Matter* **14** (18): 3497–3503. https://doi.org/10.1039/C7SM02458D.

Kam, S. I. 2008. Improved Mechanistic Foam Simulation with Foam Catastrophe Theory. *Colloids Surf A: Physicochem Eng Aspects* **318** (1–3): 62–77. https://doi.org/10.1016/j.colsurfa.2007.12.017.

Kam, S. I., Nguyen, Q. P., Li, Q. et al. 2007. Dynamic Simulations With an Improved Model for Foam Generation. *SPE J.* **12** (01): 35–48. https://doi.org/10.2118/90938-PA.

Khatib, Z. I., Hirasaki, G. J., and Falls, A. H. 1988. Effects of Capillary Pressure on Coalescence and Phase Mobilities in Foams Flowing Through Porous Media. *SPE Res Eng* **3** (3): 919–926. https://doi.org/10.2118/15442-PA.

Kil, R. A. . A., Nguyen, Q. P. . P., and Rossen, W. R. . R. 2011. Determining Trapped Gas in Foam From Computed-Tomography Images. *SPE J.* **16** (1): 24–34. https://doi.org/10.2118/124157-PA.

Kovscek, A. R. and Bertin, H. J. 2003. Foam Mobility in Heterogeneous Porous Media. *Transp Porous Med* **52** (1): 17–35.

Kovscek, A. R. and Radke, C. J. 1994. Fundamentals of Foam Transport in Porous Media, Chapter 3. In *Foams: Fundamentals and Applications in the Petroleum Industry*, ed. L. L. Schramm, 115–163. Washington, D.C., USA: ACS. https://doi.org/10.1021/ba-1994-0242.ch003.

Kovscek, A. R., Patzek, T. W., and Radke, C. J. 1994. Mechanistic Prediction of Foam Displacement in Multidimensions: A Population Balance Approach. Paper presented at the SPE/DOE Improved Oil Recovery Symposium, Tulsa, Oklahoma, 17−20 April. https://doi.org/10.2118/27789-MS.

Kovscek, A. R., Patzek, T. W., and Radke, C. J. 1995. A Mechanistic Population Balance Model for Transient and Steady-State Foam Flow in Boise Sandstone. *Chem Eng Sci* **50** (23): 3783–3799. https://doi.org/10.1016/0009-2509(95)00199-F.

Lima, N., Paciornik, S., and Carvalho, M. 2021. Foam Generation During Gas Invasion of a Porous Medium Saturated with Surfactant Solution. Paper presented at the 26th International Congress of Mechanical Engineering, Virtual. https://doi.org/10.26678/ABCM.COBEM2021.COB2021-0770.

Marsden and Khan, S. 1966. The Flow of Foam Through Short Porous Media And Apparent Viscosity Measurements. *Soc of Pet Eng J* **6** (1): 17–25.

2020. Modeling and Experimental Validation of Rheological Transition During Foam Flow in Porous Media. *Transp Porous Med* **131** (1): 315–332. https://doi.org/10.1007/s11242-019-01251-9.

Nguyen, Q. P., Rossen, W. R., Zitha, P. L. J. et al. 2009a. Determination of Gas Trapping With Foam Using X-Ray Computed Tomography and Effluent Analysis. *SPE J.* **14** (02): 222–236. https://doi.org/10.2118/94764-PA.

Nguyen, Q. P., Zitha, P. L. J., Currie, P. K. et al. 2009b. CT Study of Liquid Diversion With Foam. *SPE Prod & Oper* **24** (01): 12–21. https://doi.org/10.2118/93949-PA.

Radke, C. J. and Gillis, J. V. 1990. A Dual Gas Tracer Technique for Determining Trapped Gas Saturation During Steady Foam Flow in Porous Media. Paper presented at the SPE Annual Technical Conference and Exhibition, New Orleans, Louisiana, 23−26 September. https://doi.org/10.2118/20519-MS.

Rossen, W. R. 2013. Numerical Challenges in Foam Simulation: A Review. Paper presented at the SPE Annual Technical Conference and Exhibition, New Orleans, Louisiana, USA, 30 September−2 October. https://doi.org/10.2118/166232-MS.

Sæle, A., Graue, A., and Alcorn, Z. P. 2022. Unsteady-State CO2 Foam Injection for Increasing Enhanced Oil Recovery and Carbon Storage Potential. *Adv Geo-Energy Res* **6** (6): 472–481. https://doi.org/10.46690/ager.2022.06.04.

Simjoo, M. 2012. *Immiscible Foam for Enhancing Oil Recovery*. PhD thesis, TU Delft, Delft, The Netherlands.

Simjoo, M. and Zitha, P. L. J. 2015. Modeling of Foam Flow Using Stochastic Bubble Population Model and Experimental Validation. *Transp Porous Med* **107** (3): 799–820. https://doi.org/10.1007/s11242-015-0468-y.

Simjoo, M., Dong, Y., Andrianov, A. et al. 2013. CT Scan Study of Immiscible Foam Flow in Porous Media for Enhancing Oil Recovery. *Ind Eng Chem Res* **52** (18): 6221–6233.

Singh, G., Hirasaki, G. J., and Miller, C. A. 1997. Dynamics of Foam Films in Constricted Pores. *AIChE J* **43** (12): 3241–3252. https://doi.org/10.1002/aic.690431212.

Tang, G.-Q. and Kovscek, A. R. 2006. Trapped Gas Fraction During Steady-State Foam Flow. *Transp Porous Med* **65** (2): 287–307. https://doi.org/10.1007/s11242-005-6093-4.

Thorat, R. and Bruining, H. 2016. Foam Flow Experiments. I. Estimation of the Bubble Generation-Coalescence Function. *Transp Porous Med* **112** (1): 53–76. https://doi.org/10.1007/s11242-016-0632-z.

Urumović, K. 2016. The Referential Grain Size and Effective Porosity in the Kozeny–Carman Model. *Hydrol Earth Syst Sci* **20** (5): 1669–1680. https://doi.org/10.5194/hess-20-1669-2016.

Vikingstad, A. K., Aarra, M. G., and Skauge, A. 2006. Effect of Surfactant Structure on Foam-Oil Interactions. Comparing Fluorinated Surfactant and Alpha Olefin Sulfonate in Static Foam Tests. *Colloids Surf A: Physicochem Eng Aspects* **279** (1–3): 105–112.

Vinegar, H. J. and Wellington, S. L. 1987. Tomographic Imaging of Three-Phase Flow Experiments. *Rev Sci Instrum* **58** (1): 96–107. https://doi.org/10.1063/1.1139522.

Yuen, H. K., Princen, J., Illingworth, J. et al. 1990. Comparative Study of Hough Transform Methods for Circle Finding. *Image Vis Comput* **8** (1): 71–77. https://doi.org/10.1016/0262-8856(90)90059-E.

Zavala, R. Q., Lozano, L. F., Zitha, P. L. J. et al. 2022. Analytical Solution for the Population-Balance Model Describing Foam Displacement. *Transp Porous Med* **144** (1): 211–227. https://doi.org/10.1007/s11242-021-01589-z.

Zitha, P. L. J. 2006. A New Stochastic Bubble Population Model for Foam in Porous Media. Paper presented at the SPE/DOE Symposium on Improved Oil Recovery, Tulsa, Oklahoma, USA, 22−26 April. https://doi.org/10.2523/98976-MS.

Zitha, P. L. J. and Du, D. X. 2010. A New Stochastic Bubble Population Model for Foam Flow in Porous Media. *Transp Porous Med* **83** (3): 603–621.

Zitha, P. L. J., Nguyen, Q. P., Currie, P. K. et al. 2006. Coupling of Foam Drainage and Viscous Fingering in Porous Media Revealed by X-Ray Computed Tomography. *Transp Porous Med* **64** (3): 301–313.

Zwillinger, D. 2002. *CRC Standard Mathematical Tables and Formulae*, 31st edition. New York: Chapman & Hall/CRC.

Appendix A

Historical Notes on Polynomial Equations. It is well known that every cubic equation $ax^3 + bx^2 + cx + d = 0$ can be simplified by a simple change of variable to the depressed cubic equation $t^3 + pt + q = 0$, with $a, b, c, d, p, q \in \mathbb{R}$, for instance. Gerolamo Cardano, in his book Ars Magna (published in 1545), states that Scipione del Ferro (6 February 1465–5 November 1526) was the first to solve the cubic equation. His method exhibits the expression $t = \sqrt[3]{q/2 + \sqrt{q^2/4 - p^3/9}} + \sqrt[3]{q/2 - \sqrt{q^2/4 - p^3/9}}$ that solves the depressed cubic equation with nonpositive discriminant $\Delta = -q^2/4 + p^3/9 \leq 0$. In fact, the same expression solves all depressed cubic equations with real coefficients, for example, in Zwillinger (2002, §2.3.2), using the concept of principal cube root that was still not developed at Cardano's time. For every negative $b^2 - a_{1/3}^3$, the terms $\sqrt[3]{b + \sqrt{b^2 - a_{1/3}^3}}$ and $\sqrt[3]{b - \sqrt{b^2 - a_{1/3}^3}}$ are complex conjugate numbers and, therefore, their sum eliminates the undesirable imaginary part.